Modular DC/DC Boost Converter for Efficient and Ripple-Free Conversion in Fuel Cell-Based Powertrains

Modular DC/DC Boost Converter for Efficient and Ripple-Free Conversion in Fuel Cell-Based Powertrains

Paolo Pilati
Dept. of Electrical, Electronic, and Information Engineering
University of Bologna
Bologna, Italy
paolo.pilati3@unibo.it

Francesco Lo Franco
Dept. of Electrical, Electronic, and Information Engineering
University of Bologna
Bologna, Italy
francesco.lofranco2@unibo.it

Vincenzo Cirimele
Dept. of Electrical, Electronic, and Information Engineering
University of Bologna
Bologna, Italy
vincenzo.cirimele@unibo.it

Valerio Mariani
Dept. of Industrial Engineering
University of Bologna
Bologna, Italy
valerio.mariani4@unibo.it

Riccardo Mandrioli
Dept. of Electrical, Electronic, and Information Engineering
University of Bologna
Bologna, Italy
r.mandrioli@unibo.it

Mattia Ricco
Dept. of Electrical, Electronic, and Information Engineering
University of Bologna
Bologna, Italy
mattia.ricco@unibo.it

***Abstract*—The need to reduce emissions in the transport sector is making fuel-cell electric vehicles an option of increasing interest. However, several problems are still associated with this type of vehicles, including high costs and reliability. This paper discusses the issues related to the effects of the current ripple on PEM-type fuel cells and how a simple converter control strategy can be adopted to mitigate it. The study considers an interleaved boost converter in relation to its modular architecture and its present wide use in the automotive sector. The effect of different powertrain design parameters on the converter and its control technique is studied. Finally, a numerical analysis of the converter's efficiency is carried out to assess the possibility of achieving ripple-free operation even when phase shedding is adopted to increase the converter efficiency at partial loads.**

***Keywords*—fuel cell, interleaved boost converter, ripple-free input current, phase shedding**

I. Introduction

Electric vehicles (EVs) have gained more interest from the public and governments in recent years due to compelling concerns about the environment and scarcity of fossil fuels. Based on this, the EU and the US are promoting public policies that aim at electrification and decarbonization of transport. In the context of these decarbonization policies, the idea of using hydrogen as an energy carrier is gaining ground. This would allow energy from renewable sources to be stored in a chemical agent that can also be transported over long distances. In recent years, much emphasis has been placed on battery electric vehicles (BEVs) for the decarbonization of transport. Hydrogen could be an alternative to BEVs as it can be used in fuel-cell electric vehicles (FCEVs).

The fuel cell (FC) is a device that produces electrical energy when continuously supplied with fuel and a combustion agent. In contrast to electrochemical batteries, FCs have several important advantages: their low weight in proportion to the power they can deliver, the energy delivered is contained in fluids that can be stored in tanks whose refueling requires little time, and the absence of phenomena of self-discharge [1]. The fuels and oxidants that can power the cells are diverse, depending on the technology used, but hydrogen and oxygen are most commonly used. Hydrogen is characterized by its high electrochemical reactivity, reacting with pure oxygen to ensure the absolute absence of pollutants emitted during electrochemical energy conversion, with water being the only product of the reaction [2]. FCs can be used as power systems for an EV mainly in two ways, as briefly shown in Fig. 1:

- by directly connecting the cell stack to the inverter that powers the electric motor (Fig. 1(a));
- in parallel with another storage system, such as batteries or supercapacitors (Fig. 1(b)).

In the direct connection, efficient operation of the electric motor requires the FC to be supplied with the same dynamics as the motor's power demand. This is not achievable in the majority of real applications because the cell's power supply depends on mechanical components (e.g., pumps, valves, etc.) whose dynamics are slower than the engine's electrical dynamics. This type of configuration therefore requires the stack to be oversized to supply the motor correctly, thus increasing volume, weight, and costs. Indeed, the parallel battery pack configuration is the most commonly used configuration [3]. This is because the battery is able to meet the power demands with dynamics compatible with those of the powertrain. This consequently allows mitigation of the power peaks required for the cell stack, which can then work with slower dynamics. Naturally, this arrangement allows a reduction in the FC stack size at a cost of the increase in the complexity of the system [4]. Finally, it is worth noting that, unlike the FC, the battery can handle power flow reversals. This allows regenerative braking

The preset work is funded by PNRR M4C2 – Investment 1.4 – Project Mobility "Sustainable Mobility Center" – Code CN00000023 - CUP: J33C22001120001.

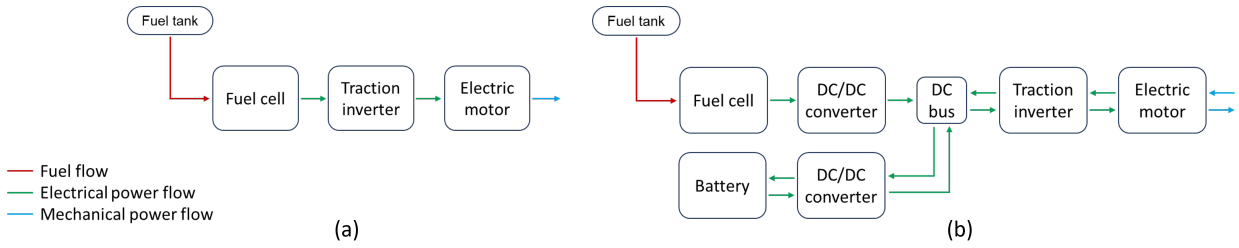

Fig. 1. Rough schematic of the powertrain of a fuel cell electric vehicle: (a) direct connection of the fuel cell to the inverter; (b) considering also another storage system in parallel.

to be used with a consequent increase in overall powertrain efficiency [5]. A more exhaustive and detailed analysis of architectures for FCEV is provided in [6].

At the moment, some of the major limitations to the deployment of this type of technology are cost and reliability. To date, the cost is highly dependent on the useful life of the FC. Its extension in fact is one of the most important aspects of research in this area [7].

II. Background and Motivation

This Section provides an overview of the technical background useful for the understanding of the main content of the work and its motivation.

A. Overview on Fuel Cell

The FC is a device that converts chemical energy directly into electrical energy. FCs, as well as batteries, are part of the group of galvanic cells. The difference between the two lies in the fact that the reagents must be supplied from outside in the former, while in the latter they are already present internally. The content of this work focuses on a specific typology of FC called proton exchange membrane (PEM). This is because PEM FC technology offers characteristics much more suitable for traction systems than other more established technologies such as, for example, alkaline FCs. The PEM cell consists of two electrodes separated by a polymer membrane able to transport only hydrogen ions that act as an electrolyte [8]. Mainly, PEM cells allow faster dynamic response and higher volumetric power density compared to alkaline FCs [7] and have almost constant efficiencies over the entire load curve making them more suitable for use in automotive applications.

As detailed in [1], the operating voltage of a fuel cell, V_{FC}, can be expressed as

$$V_{\mathrm{FC}} = E_0 - V_{\mathrm{act}}(i) - V_{\Omega}(i) - V_{\mathrm{conc}}(i) \ , \qquad (1)$$

where E_0 is the so-called Nernst voltage, V_{act} is the voltage drop due to activation losses, V_{Ω} is the voltage drop due to ohmic losses, and V_{conc} the one due to concentration losses [1]. The Nernst voltage can be assumed as the open-circuit voltage of the FC while these last three voltage drops are associated with non-idealities due to the chemistry of the reaction and depend on the current flowing through the stack. Based on the current (and thus the power), one or more effects may be neglected by the others. Activation and concentration drops have a non-linear pattern, so FCs are designed to work in the region of ohmic drops, where the voltage at the ends of the stack varies linearly with the current.

B. Effects of Current Ripple on the Fuel Cell

One of the main problems associated with PEM technology seems to be the effect that the current ripple has on the polymer membrane. Variations in the current cause changes in the flow rates of fluids entering and leaving the membrane, causing mechanical stress that leads to membrane degradation.

In [9], an analysis of the effects of ripple at different frequencies (100 Hz, 1 kHz, and 10 kHz) based on electrochemical impedance spectroscopy was made. The test was done on 12 single-cell PEM FCs using a square wave current with a mean value of 20 A. It is shown that the low-frequency current ripple accelerates the PEM FC degradation. The effect of high-frequency ripple on PEM cells is analyzed in [10]. An endurance test of 2600 hours was carried out on 2 single-cell PEM FCs to asses aging using a 20 kHz triangular current waveform. In this case, an increase in activation losses was found. In [11], the effect of different types of waveforms (sinusoidal, triangular, and square) and frequencies, up to 1 kHz, was studied on a single-cell configuration. In the article, the researchers found that low frequencies in particular cause the greatest reduction in efficiency, which was attributed to the non-linear response of the polarisation curve. In [12], the effect of low-frequency ripple on a 300 W FC was studied, showing that this affects both the useful life and efficiency of the FC. In the article, it is hypothesized that the reduction in efficiency is the cause of the reduction in useful life. There have been many other studies about power electronics for PEM FCs [13], in which, however, ripple minimization is achieved through the development of unconventional converter topologies. The present work aims instead to explore the use of an already-known modular architecture, the interleaved boost converter, by investigating its properties and control.

C. Interleaved Boost Converter and Zero-Ripple Strategy

An FC stack is generally not able to provide an adequate voltage level to supply the traction inverter. The voltage level of the DC bus currently stands at 400 V, which is also the typical voltage for traction battery packs. Recently, however, powertrains with a DC bus voltage level of 800 V have also begun to appear. It is therefore necessary to introduce a boost

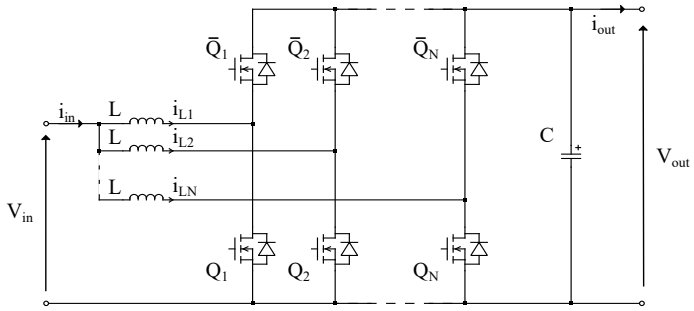

Fig. 2. Generic circuit diagram of an interleaved synchronous boost converter with N legs.

DC/DC converter to match the output voltage of the FC to the DC bus levels of the powertrain. The chosen topology for this article is the one of synchronous interleaved boost converter. Its circuit diagram is shown in Fig. 2.

This kind of converter has been already proposed for FC applications in the automotive sector [13]. In this paper, this structure is investigated in conjunction with the control strategy proposed in [14], with the aim of achieving a ripple-free current on the input side of the converter.

In the synchronous interleaved boost the input current is shared between all operating legs. Considering an N-leg converter, the phase of each leg current is evenly shifted by an electric angle equal to $360°/N$. The upper and lower switches of each leg operate in a complementary manner.

Equation (2) expresses the peak-to-peak ripple pattern of the input current $\Delta i_{\mathrm{in,pp}}$ for any operating condition:

$$\Delta i_{\mathrm{in,pp}} = \frac{V_{\mathrm{in}}}{L f_{\mathrm{sw}}}\left[1 - N\left(D - \frac{p-1}{N}\right)\right]\left(D - \frac{p-1}{N}\right) \ , \quad (2)$$

where f_{sw} is the switching frequency, L is the inductance on each leg of the converter and p is the integer number obtained from the approximation by the excess of the product $N \cdot D$.

Based on (2), depending on the chosen duty cycle, there are $N + 1$ points in which it is possible to obtain a zero input current ripple. Even if from the outside there are points at which it is possible to achieve zero ripple on the input current, there is always a current ripple in the individual legs. The peak-to-peak leg current ripple Δi_{Lpp} can be calculated as:

$$\Delta i_{\mathrm{Lpp}} = \frac{V_{\mathrm{in}}}{L f_{\mathrm{sw}}}(1 - D)D \ . \quad (3)$$

Equation (3) shows that, except in cases where there is no switching (i.e., D equal to 0 or 1), there is always a current ripple on the leg inductor.

III. Design of the Converter

The analysis of the converter is carried out by assuming the configuration shown in Fig. 1(b), in which the FC's DC/DC converter is connected to the DC bus of the whole powertrain.

The idea behind the proposed technique was presented in [15]. In that work, the technique was developed for a buck converter used for EV charging applications. In this case, the concept has been adapted and modified to fit this specific application. In addition, the specific goal of current ripple cancellation is related here to that of the maximization of conversion efficiency. The goal is to test within what limits the conversion efficiency can be improved while always ensuring no ripple on the FC current.

The considered technique aims at maintaining a fixed duty cycle as the input voltage of the converter changes. This allows the ripple-free condition to be maintained within a certain permissible range of output voltage variation. In the design of the converter, the voltage V_{FC} as well as the current provided by the FC depend on the characteristics of the FC. The output voltage is the one of the DC bus that, to a certain extent, is assumed as a degree of freedom. Given the limits of the output voltage, the minimum number of legs N_{min} required to achieve ripple-free operation can be calculated as:

$$N_{\mathrm{min}} = \mathrm{ceil}\left(\frac{V_{\mathrm{out,min}}}{V_{\mathrm{in,min}}}\right) \ . \quad (4)$$

The lower limit of the output voltage V_{out} can be imposed based on the modulation index of the inverter and the configuration of the DC/DC connected to the battery. At this point, the upper limit still needs to be defined. The greater the margin of the output voltage, the greater the possibility of implementing ripple-free even with a reduced number of legs. But an oversizing of the voltage rating of the switch will also be required. A tighter limit would require more legs in the converter to ensure ripple-free over the entire input voltage range. With the same chosen limits, increasing the number of legs allows extending the duty cycle values that can be used. It is worth highlighting that a high number of legs also allows for greater reliability of the converter. In case of failure of one switch, the converter can continue to operate even if with a derating of the power.

Silicon Carbide (SiC) MOSFETs are assumed to be used for the converter. In fact, switches based on such technology have lower switching losses and lower conduction resistance compared to traditional silicon (Si) devices [16]. In addition, MOSFETs allow higher switching frequencies than IGBTs, thus reducing the size of the inductors. IGBTs are better suited to conducting high currents. However, as the total load current is spread over N legs, there is no need for each leg to conduct high currents. For these reasons, SiC MOSFETs are considered in the efficiency calculation.

The overall efficiency η_{tot} of the system can be calculated as the product of the two individual efficiencies of the FC η_{FC} and of the converter η_{conv}, as in (5):

$$\eta_{tot} = \eta_{\mathrm{FC}} \cdot \eta_{\mathrm{conv}} \ . \quad (5)$$

The efficiency of the FC versus the provided power P_{FC} has been extrapolated from a typical efficiency curve found in the literature [12] and rescaled based on a reference value for this case. As can be seen from Fig. 3, the efficiency exhibits fairly constant behavior over the entire power range with a maximum around lowest values.

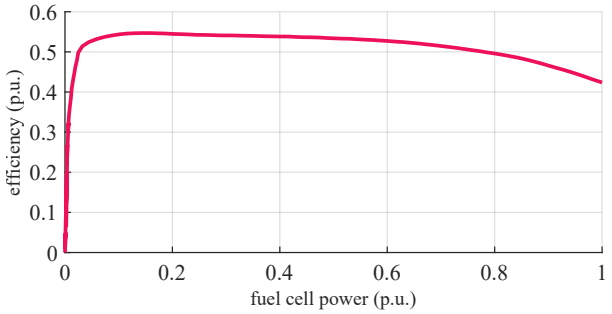

Fig. 3. Example of a fuel cell's efficiency trend as a function of power output ratio.

The efficiency of the converter can be calculated as the ratio between the output power P_{out} and the input power P_{FC}. Considering all legs of the converter equal, the losses within the individual leg can be divided into losses in the inductor P_{L} and those in the switches P_{sw}. Hence, considering all the N legs of the converter equal, the converter losses can be expressed as:

$$P_{\text{out}} = P_{\text{FC}} - N(P_{\text{L}} + P_{\text{sw}}) \ . \tag{6}$$

In turn, P_{L} are divided into losses in the ferromagnetic core P_{Fe} and losses in the copper P_{Cu}, as in (7):

$$P_{\text{L}} = P_{\text{Fe}} + P_{\text{Cu}} \ . \tag{7}$$

For the sake of simplification, the losses in the ferromagnetic core of the inductor are calculated by using the Steinmetz equation (see, [17]):

$$P_{\text{Fe}} = m_{\text{Fe}} k f_{\text{sw}}^{m} \hat{B}^{n} \ , \tag{8}$$

in which $\hat{B}$ is the peak magnetic flux density in the inductor core, m_{Fe} is the ferromagnetic core weight, k, m, and n are coefficients that depend on the type of material used to make the ferromagnetic core. The variable f_{sw} represents the switching frequency, which is the same as the leg current ripple. $\hat{B}$ is directly proportional to the peak current of the inductor. Therefore, once the appropriate inductor has been chosen and the switching frequency fixed, the losses in the inductor core can be scaled as a function of the current.

The copper losses are considered equal to

$$P_{\text{Cu}} = i_{\text{L,rms}}^{2} R_{\text{L}} \ , \tag{9}$$

being R_{L} the resistance of the inductor windings.

The losses P_{sw} associated with a switch are considered as the sum of conduction losses P_{Ω}, commutation losses P_{com}, and a component P_{aux} representing the power required by the MOSFET drivers:

$$P_{\text{sw}} = P_{\Omega} + P_{\text{com}} + P_{\text{aux}} \ . \tag{10}$$

The power absorbed by the auxiliary circuits is approximated as independent of the current flowing through the switch. Thus, the power $P_{\text{aux,i}}$ absorbed by the auxiliaries for each switch is considered constant. So, the total power absorbed by the auxiliaries depends only on the number of active switches, as per:

$$P_{\text{aux}} = 2P_{\text{aux,i}}N \ . \tag{11}$$

Within the single leg, the lower switch conducts for a fraction of the switching period equal to D. For the remaining fraction, i.e., $D-1$, the upper leg diode conducts. Thus, conduction losses can be defined as:

$$P_{\Omega} = i_{\text{L,rms}}^{2} R_{\text{sw,on}} D + (i_{\text{L,rms}} V_{\text{d}} + i_{\text{L,rms}}^{2} R_{\text{d}})(D-1) \ , \tag{12}$$

where $R_{\text{sw,on}}$ is the switch on-state resistance, V_{d} is the diode forward voltage, and R_{d} is the diode on-state resistance. The reference values for the energy dissipated during the commutation of individual switch are extracted from the component datasheets. Indeed, the energy values provided generally refer to a precise voltage and current condition i_{rate} applied to the switch and vary linearly with the current flowing through the switch. As a first approximation, the only effect of the current is considered hence the value of dissipated energy provided in the datasheet is rescaled only on the basis of the current flowing through the switch. Thus commutation losses can be expressed as:

$$P_{\text{com}} = f_{\text{sw}}(E_{\text{on}} + E_{\text{off}}) \frac{i_{\text{L,rms}}}{i_{\text{rate}}} \ , \tag{13}$$

where E_{on} and E_{off} are the energy dissipated during switching turn-on and turn-off, respectively.

A technique used to improve the efficiency of an interleaved converter is phase shedding. If the converter operates at partial load, a reduced number of legs is used to reduce losses. In the following sections, the feasibility of this technique while implementing ripple-free will be investigated.

IV. Analysis and Numerical Validation

In this section, a numerical example is provided to test the functioning of the proposed architecture and the applied ripple-free technique. The analysis is carried out by means of circuit simulation based on PLECS environment.

The nominal, minimum, and maximum values of the quantities considered for converter sizing are summarized in Table I. These values are reported as a range to take into account the entire permissible load range of the FC that does not operate at a fixed point. The DC bus voltage is chosen in the range $600-800$ V. The choice of the lower limit is such that if the battery had a nominal voltage of 400 V, its maximum voltage would in any case be lower than the minimum of the DC bus. This in order to allow a possible battery DC/DC (see Fig. 1(b))

TABLE I
Converter Design Data

Parameter	Nominal	Min	Max	Unit
V_{in}	260.0	240.0	360.0	V
i_{in}	360.0	0.0	530.0	A
P_{in}	93.6	0.0	127.2	kW

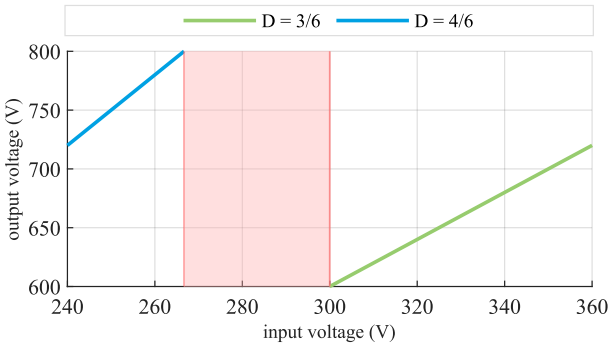

(a)

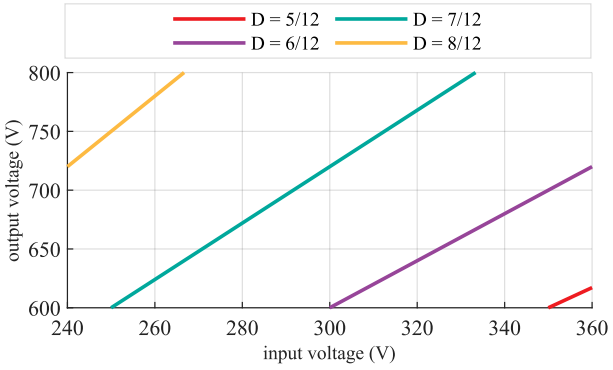

(b)

Fig. 4. Comparison between different numbers of legs with the same output voltage limits: (a) case with $N = 6$; (b) case with $N = 12$.

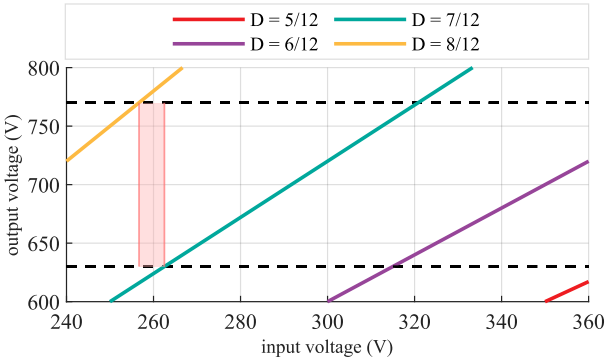

Fig. 5. Comparison between different output voltage limits (the dashed lines refer to tighter limits) with the same number of legs $N = 12$.

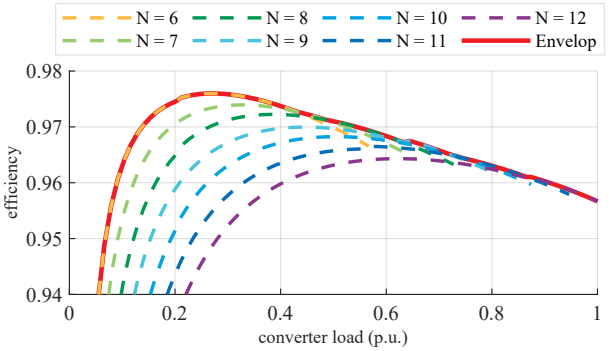

Fig. 6. Efficiency curves varying the number of legs from $N = 6$ to $N = 12$ and their upper envelope.

to function either as a buck or a boost according to the power flow. The upper limit, on the other hand, would allow 1200 V switches to be operated at a utilization factor of 60-70%, thus guaranteeing a certain safety margin.

For the calculation of converter efficiency, the STMicroelectronics SCTH60N120G2-7 MOSFET is chosen as the model for switches. The switching frequency f_{sw} is considered fixed and equal to 50 kHz.

The adopted values of the Steinmetz model considered for the rescaling of the losses in the inductor are $k = 1.983 \cdot 10^{-3}$, $m = 1.36$, and $n = 2.86$. These values are typical reference values for ferrite cores [17]. The considered inductor winding resistance is $R_{\mathrm{L}} = 35\ \mathrm{m\Omega}$. The reference core losses assumed at the rated conditions for the inductor are $P_{\mathrm{Fe}} = 72.5$ W. The power $P_{\mathrm{aux,i}}$ absorbed by the auxiliaries for each switch is assumed to be a typical value of 5 W.

Based on (4), the minimum number of legs needed to obtain ripple-free operation is equal to 3. The minimum number of legs, however, cannot guarantee ripple-free over the entire range of possible input voltages. In this case, therefore, 12 legs were chosen. This allows to have currents of up to around 45 A on each leg of the converter, thus enabling the use of smaller components. In Fig. 4 it can be seen how a reduced number of legs, with the same output voltage limits, may not satisfy the ripple-free operation for every load condition. With the output voltage limits imposed, ripple-free operation can be guaranteed by using a number of legs between 7 and 12.

The considerations made regarding the choice of the DC bus voltage limits can be summarized as in Fig. 5. It can be seen how a choice of stricter limits (dotted lines) can lead to the inability to operate no ripple on all load conditions, despite the same number of legs. For instance, in the highlighted area around 260 V input no duty cycle can satisfy the ripple-free condition.

The results in terms of efficiency for the different numbers of operating legs are shown by means of Fig. 6. As can be seen, the efficiency increases as the number of active legs decreases. At maximum load, the efficiency of the converter is just below 96%, while at low loads it drops dramatically due to the fixed contributions taken into account in the calculation of losses. For a number of legs lower than 7, the technique's operation cannot be guaranteed over the entire range of possible input voltages. In Fig. 4(a), the highlighted area indicates where there are no duty cycles that guarantee ripple-free.

To test the phase shedding of the converter combined with the ripple-free technique, a 5 s load ramp of the FC has been simulated with the trend shown in Fig. 7. The effect that phase shedding combined with the ripple-free technique have on the waveforms of the currents flowing through the different active legs can be appreciated in Fig. 8. As proven in Fig. 9, the current flowing through the FC is free of any ripple. The sections detailed in both figures refer to two switching periods. The current and power peaks are due to the insertion transients of the new legs and the consequent instantaneous distortion in the duty cycle. In real mission profiles, leg insertion is performed gently avoiding any transient; such a topic is outside current paper's scope.

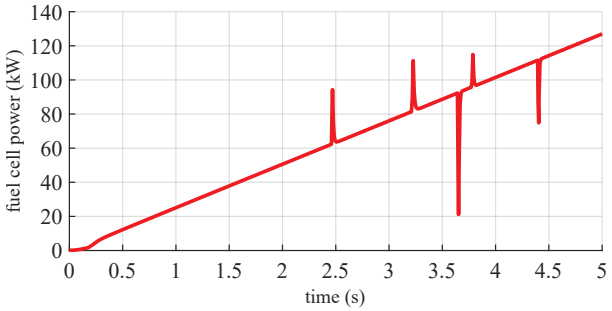

Fig. 7. Trend of the power delivered by the fuel cell during the simulation interval.

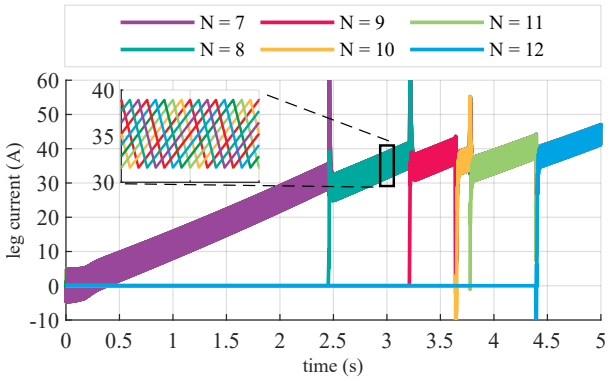

Fig. 8. Current in the different legs and details of two switching periods of the highlighted section.

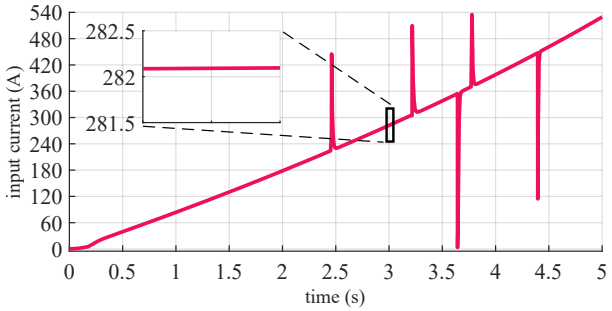

Fig. 9. Input current and details of two switching periods of the highlighted section.

V. Conclusions

In this paper, the problem of the current ripple concerning fuel cells was examined. Using an interleaved boost type converter, the possibility to cancel the ripple on the input current was proven. By cancelling the ripple on the current delivered by the fuel cell, its life can be preserved and extended. In addition, it was observed how the choice of DC bus voltage limits and the number of legs affect the effectiveness of the technique discussed. Finally, an efficiency study of the considered converter was done. Phase shedding has proven to be a valid option to increase the efficiency of the converter and thus of the entire system at partial loads. If phase shedding leads to loss the ripple-free operation, a choice must be made between continuing to maintain the ripple-free condition or preferring to maintain high conversion efficiency. Further future research developments will focus on a refinement of the efficiency calculation and on the proper management of the transients to reduce current peaks.

References

[1] G. Kaur, *PEM fuel cells: fundamentals, advanced technologies, and practical application*. Elsevier, 2021.

[2] EG&G Technical Services, Inc, *Fuel Cell Handbook (Seventh Edition)*, US Department of Energy, Office of Fossil Energy, National Energy Technology Laboratory, USA, West Virginia, Morgantown, Ed. Lulu.com, 2004.

[3] P. Fragiacomo, M. Genovese, F. Piraino, O. Corigliano, and G. De Lorenzo, "Hydrogen-fuel cell hybrid powertrain: conceptual layouts and current applications," *Machines*, vol. 10, no. 12, p. 1121, 2022.

[4] I.-S. Sorlei, N. Bizon, P. Thounthong, M. Varlam, E. Carcadea, M. Culcer, M. Iliescu, and M. Raceanu, "Fuel cell electric vehicles—a brief review of current topologies and energy management strategies," *Energies*, vol. 14, no. 1, p. 252, 2021.

[5] M. Ehsani, Y. Gao, S. Longo, and K. Ebrahimi, *Modern electric, hybrid electric, and fuel cell vehicles*. CRC press, 2018.

[6] S. Liu, Y. Bin, Y. Li, and B. Scheppat, "Hierarchical mpc control scheme for fuel cell hybrid electric vehicles," *IFAC-PapersOnLine*, vol. 51, no. 31, pp. 646–652, 2018.

[7] M. M. Tellez-Cruz, J. Escorihuela, O. Solorza-Feria, and V. Compañ, "Proton exchange membrane fuel cells (pemfcs): Advances and challenges," *Polymers*, vol. 13, no. 18, p. 3064, 2021.

[8] B. Paul and J. Andrews, "Pem unitised reversible/regenerative hydrogen fuel cell systems: State of the art and technical challenges," *Renewable and Sustainable Energy Reviews*, vol. 79, pp. 585–599, 2017.

[9] J. Kim, I. Lee, Y. Tak, and B. Cho, "Impedance-based diagnosis of polymer electrolyte membrane fuel cell failures associated with a low frequency ripple current," *Renewable energy*, vol. 51, pp. 302–309, 2013.

[10] T. Jarry, A. Jaafar, C. Turpin, F. Lacressonniere, E. Bru, O. Rallieres, and M. Scohy, "Impact of high frequency current ripples on the degradation of high-temperature pem fuel cells (ht-pemfc)," *International Journal of Hydrogen Energy*, 2023.

[11] H. P. Buitendach, R. Gouws, C. A. Martinson, C. Minnaar, and D. Bessarabov, "Effect of a ripple current on the efficiency of a pem electrolyser," *Results in Engineering*, vol. 10, p. 100216, 2021.

[12] Y. Zhan, Y. Guo, J. Zhu, B. Liang, and B. Yang, "Comprehensive influences measurement and analysis of power converter low frequency current ripple on pem fuel cell," *International Journal of Hydrogen Energy*, vol. 44, no. 59, pp. 31 352–31 359, 2019.

[13] M. İnci, M. Büyük, M. H. Demir, and G. İlbey, "A review and research on fuel cell electric vehicles: Topologies, power electronic converters, energy management methods, technical challenges, marketing and future aspects," *Renewable and Sustainable Energy Reviews*, vol. 137, p. 110648, 2021.

[14] K. Drobnic, G. Grandi, M. Hammami, R. Mandrioli, M. Ricco, A. Viatkin, and M. Vujacic, "An output ripple-free fast charger for electric vehicles based on grid-tied modular three-phase interleaved converters," *IEEE Transactions on Industry Applications*, vol. 55, no. 6, pp. 6102–6114, 2019.

[15] R. Mandrioli, M. Ricco, M. Hammami, A. Viatkin, and G. Grandi, "A ripple-free output current interleaved dc/dc converter design algorithm for ev charging," in *2021 22nd IEEE international conference on industrial technology (ICIT)*, vol. 1, 2021, pp. 292–297.

[16] L. F. Alves, P. Lefranc, P.-O. Jeannin, and B. Sarrazin, "Review on sic-mosfet devices and associated gate drivers," in *2018 IEEE International Conference on Industrial Technology (ICIT)*, 2018, pp. 824–829.

[17] C. W. T. McLyman, *Transformer and inductor design handbook*. CRC press, 2004.